https://doi.org/10.5194/egusphere-2026-3012
Preprint. Discussion started: 16 June 2026

Detecting Fault Structures from Earthquake Sequences via Unsupervised Learning

Kuan-Ting Tu, Ming-Wey Huang, Siao-Syun Ke

National Science and Technology Center for Disaster Reduction, New Taipei City, Taiwan, R.O.C.

Correspondence to: Ming-Wey Huang (mwhuang@ncdr.nat.gov.tw)

Abstract. This study develops a systematic framework to detect potential fault structures from earthquake sequences by integrating unsupervised learning and three-dimensional spatial analysis. Two major events in eastern Taiwan, EQ2018 and EQ2024, are analyzed using DBSCAN clustering, validated by the Silhouette Score, followed by Principal Component Analysis (PCA) to extract fault-plane geometries. The clustering results reveal both mapped and previously unrecognized fault orientations, with PCA-derived planes largely consistent with centroid moment tensor solutions of the largest-magnitude events. EQ2018 ruptures were confined to shallow crustal levels (<20 km), dominated by west-dipping planes, whereas EQ2024 exhibited greater depth variability, multiple dipping directions, and complex rupture geometries involving both onshore and offshore fault systems. Three-dimensional visualization further highlights the interplay between known active faults (e.g., Central Range, Milun, Lingding) and latent structures, underscoring the heterogeneous nature of rupture propagation in tectonically transitional zones. While PCA effectively captures dominant planar trends, limitations remain in representing curved or arc-shaped geometries. Overall, the proposed workflow demonstrates the utility of combining clustering and PCA to delineate subtle fault structures, offering a robust tool for advancing seismotectonic interpretation and improving seismic hazard assessment.

1 Introduction

Following a major earthquake, regional stress redistribution commonly induces sequences of aftershocks that re-equilibrate the crustal stress field. The spatial distribution of these aftershocks is often used to delineate the rupture zone of the mainshock, and stress transfer may further activate structurally weak surfaces, generating additional seismic events (King et al., 1994; Stein, 1999; Freed, 2005; Toda et al., 2005). Yet, rupture processes of large earthquakes are inherently complex; multiple faults may rupture simultaneously (Liu et al., 2019; Jia et al., 2023; Petersen et al., 2023), complicating the correspondence between seismic activity and mapped geological structures.

The characterization of subsurface fault systems has traditionally relied on geological surveys and geophysical investigations, including seismic event distribution, focal mechanism analysis, seismic wave exploration, and tomographic imaging (Font et al., 2001; Shyu et al., 2005; Wu et al., 2009; Huang et al., 2022). These approaches have provided valuable insights into regional tectonics and guided interpretations of structural planes. However, the objective and automated reconstruction of fault-plane geometries from discrete seismicity remains a major challenge. Conventional interpretations often depend on expert judgment, which introduces subjectivity and limits reproducibility. Recent advances in computational geoscience, such as machine learning and probabilistic modelling, offer promising pathways to overcome these limitations.

Unsupervised algorithms have been increasingly applied to the analysis of earthquake catalogs. Ouillon et al. (2008) proposed a pattern recognition method based on the k-means technique to reconstruct the 3D structure of active fault networks using earthquake hypocenter data. The Density-Based Spatial Clustering of Applications with Noise (DBSCAN) (Ester et al., 1996) has proven effective in handling the irregular geometries and noisy characteristics of aftershock distributions (Fan and Xu, 2019; Herrmann et al., 2022; Bariklana and Fauzan, 2023). In addition, Principal Component Analysis (PCA) (Savage, 1988) provides a means of identifying the dominant linear trends that represent the greatest variance in earthquake distributions. These trends may implicitly reflect underlying geological features and can assist in the classification of seismic attributes and structural interpretation (Roden et al., 2015; Quinn and Ehlmann, 2019).

Several studies have employed diverse unsupervised learning techniques to delineate potential fault structures. Jian and Wang (2022) applied both DBSCAN and PCA to characterize seismic activity and cluster trends, thereby inferring latent structural orientations. Building on similar approaches, Piegari et al. (2024) introduced a hierarchical segmentation workflow in which DBSCAN was first applied to identify major fault planes, the analytic method of ordering points to identify the clustering structure (OPTICS; Ankerst et al., 1999) was employed for secondary clustering, and PCA was employed to compute trend surfaces and define segmented geometries. Although these studies demonstrate the utility of long-term earthquake catalogs for regional structural analysis, they remain limited in establishing causal linkages between principal fault planes and adjacent latent structures that may be activated by mainshock events.

This limitation is exemplified by two damaging earthquakes that occurred north of Hualien, eastern Taiwan, in 2018 and 2024, which resulted in casualties, infrastructure damage, and economic losses (Lin et al., 2019; Lin et al., 2020; Lin and Wu, 2025). Both events were followed by abundant aftershocks shortly after the main shocks. Numerous studies have highlighted the intricate rupture mechanisms associated with these events (Huang and Huang, 2018; Yen et al., 2019; Tung et al., 2019; Lee et al., 2025; Lin and Wu, 2025). Nevertheless, systematic quantitative analyses of aftershock clustering in three-dimensional space and their associations with multiple rupture planes remain scarce.

Notably, the aftershocks of the 2018 and 2024 events were distributed not only along the principal rupture plane but also in adjacent regions, exhibiting distinct clustering phenomena. Preliminary visual inspection suggests the presence of multiple rupture geometries, underscoring the need for rigorous spatial analyses to clarify the relationship between aftershock sequences and complex fault structures. Such analyses would provide critical insights into seismic triggering mechanisms and structural connectivity in collision-boundary environments, thereby advancing both theoretical understanding and practical hazard assessment.

Accordingly, this study applies DBSCAN to three-dimensional clustering of aftershock sequences, aiming to investigate their spatial and structural features. Building on the DBSCAN-derived clusters, this study employs PCA to infer the geometric distribution of potential rupture planes. Through the integration of three-dimensional clustering and principal component analysis, this research seeks to characterize the spatial properties of aftershock sequences and to hypothesize the geometry of seismogenic structures and potential rupture surfaces. The findings not only contribute to clarifying the relationship between complex earthquake sequences and regional tectonics but also provide a foundation for subsequent geological modeling and seismic hazard assessment, with potential applications in regional disaster risk reduction planning.

2 Study Area and Data

2.1 Study area: Geological Setting and Tectonic Framework of Eastern Taiwan

Taiwan lies at the convergent boundary between the Philippine Sea Plate (PSP) and the Eurasian Plate (EP), a tectonic setting that produces complex geological structures and frequent seismic activity in its eastern region. Analyses based on Global Positioning System (GPS) data indicate that the PSP converges northwestward toward the EP at an estimated velocity of 82 mm per year (Yu et al., 1997). Within this framework, the Longitudinal Valley (LV) of eastern Taiwan represents a suture zone formed by plate collision and constitutes one of the island’s most significant active tectonic regions.

Figure 1 illustrates the tectonic framework of the study area and the spatial distribution of aftershocks. Four major active faults are identified in Figure 1a: the east-dipping Milun Fault, the Longitudinal Valley Fault system (LVF; including the Linding Faults), and the west-dipping Central Range Fault (CRF). The LV hosts several significant active structures, notably the Milun Fault, the LVF, and the CRF (Lin et al., 2021; Chen et al., 2024). Offshore tectonic features are primarily associated with the Ryukyu subduction system (Suppe, 1984).

The Milun Fault, located at the northern tip of the valley, extends 8 km on land and 21 km in total length, with a depth of 10 km. It dips steeply eastward at about 75° and exhibits left-lateral strike-slip motion with a reverse component (Hsu, 1956; Shyu et al., 2005; Shyu et al., 2016). The LVF, situated between the Coastal Range and the Backbone Range, is dominated by reverse and left-lateral strike-slip faulting, with an eastward dip. Based on seismic activity, the LVF can be subdivided into several segments from north to south: the Lingding, Rueyshui, Chihshang, Lichi, and Luyeh faults (Chen et al., 2007; Shyu et al., 2016; Chen et al., 2024).

In contrast, the CRF has long lacked definitive structural evidence from field surveys, geomorphic analyses, and drilling studies (Tsai, 1986; Rau and Wu, 1998; Chen et al., 2007). Recent seismicity in the LV, supported by focal mechanisms and aftershock distributions, points to a west-dipping fault system (Wu et al., 2006; Chuang et al., 2014; Wen et al., 2019; Tang et al., 2023). Seismic catalogs, focal mechanism analyses, and tomography likewise suggest a west-dipping CRF along the eastern flank of the Backbone Range (Huang and Wang, 2022; Chen et al., 2024). These findings imply several possible geometries: a single throughgoing interface, imbricate thrusts, or segmented-parallel faults. Each carries distinct kinematic implications for dip variation, segmentation, and strain partitioning. Resolving among them requires integrated constraints from microseismicity, geodetic inversions, balanced cross-sections, and targeted drilling, ultimately advancing the CRF toward a coherent structural framework.

Collectively, these observations highlight the coexistence of multiple interacting fault systems and complex geometrical structures in the LV. Such complexity challenges the adequacy of single-structure models in explaining the spatial distribution of earthquake sequences. To address this issue, the present study focuses on the LV region and employs three-dimensional spatial analysis of aftershock sequences to reassess the potential seismogenic structures reflected in recent seismic activity.

2.2 Seismic Sequence Data and Aftershock Characteristics

High-density seismic sequence data provide an effective means of delineating subsurface rupture structures through spatial distribution analysis. In the study area, two major earthquake events occurred in 2018 (hereafter referred to as EQ2018) and 2024 (hereafter referred to as EQ2024) (Table 1), with mainshock magnitudes of M_L 6.26 and M_L 7.19, respectively. Both events produced abundant aftershocks (Central Weather Administration, CWA, refer to https://scweb.cwa.gov.tw/en-us/earthquake/data, last accessed on 13 January 2026; CWA, 2012), characterized by pronounced spatial clustering. Beyond ruptures directly associated with the mainshocks, visual inspection further indicates the presence of subsidiary rupture surfaces. Cheng et al. (2015) reported that the magnitude of completeness (M_c) for the Taiwan earthquake catalog ranges between 2.0 and 3.0. To ensure the reliability of clustering analyses, this study considers seismic events with local magnitudes (M_L) $\geq$ 3.0 occurring within 30 days after each mainshock, as shown in Figure 1b. After filtering, the aftershock sequences comprise 491 events for EQ2018 and 2,373 events for EQ2024.

Notably, the depth distributions reveal contrasting patterns: EQ2018 aftershocks are concentrated within shallow crustal levels, whereas EQ2024 aftershocks span from shallow to greater depths. This divergence underscores distinct rupture mechanisms between the two events. Specifically, the shallow confinement of EQ2018 aftershocks suggests a localized rupture process primarily affecting upper crustal structures, while the broader depth range of EQ2024 indicates a more complex rupture propagation that penetrated deeper lithospheric levels. Such differences not only reflect variations in fault geometry and stress release but also imply contrasting potentials for energy transfer and secondary fault activation.

Figure 2 illustrates the daily aftershock counts for both events. For EQ2018 (Figure 2a), more than 250 aftershocks occurred on the day of the mainshock (Day 0), marking the peak, followed by a gradual decline in activity over subsequent days. In contrast, EQ2024 (Figure 2b) recorded over 700 aftershocks on Day 0, again representing the maximum. The sequence then decreased with time; however, unlike EQ2018, EQ2024 exhibited a pronounced secondary peak on Day 19 (April 22, 2024), when aftershock activity surged before resuming its overall declining trend. The spatial distribution shown in Figure 1b further highlights differences between the two periods: earthquakes in the second sequence are concentrated in the southern region, whereas only scattered events are observed in the north.

This temporal and spatial contrast suggests that EQ2018 followed a relatively typical decay pattern consistent with Omori's law (Omori, 1894), while EQ2024 displayed more complex dynamics, potentially reflecting delayed stress release or secondary fault activation. The southern concentration of EQ2024 aftershocks may indicate localized stress redistribution along adjacent fault systems, underscoring the heterogeneous nature of rupture propagation. These findings emphasize the importance of integrating temporal clustering with spatial analysis to better understand aftershock evolution and its implications for seismic hazard assessment.

Table 1. Two events information

Origin time (local time, UTC + 8)	Magnitude (M_L)	Longitude (degree)	Latitude (degree)	Depth (km)
2018/02/06 23:50	6.26	121.73	24.1	6.3
2024/04/03 07:58	7.19	121.57	23.88	19.7

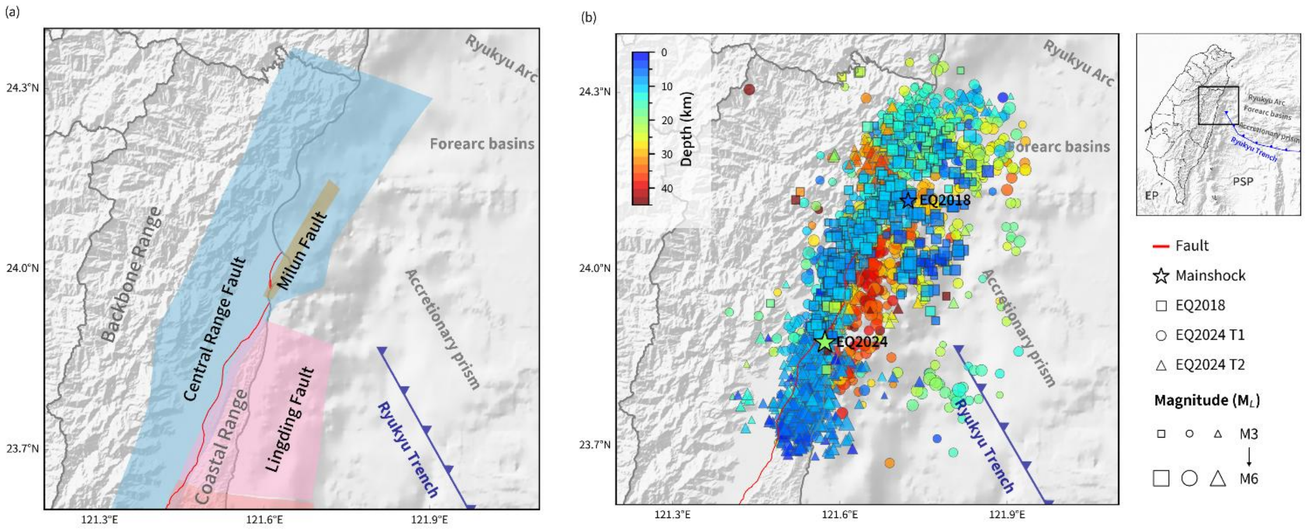

Figure 1: Study area. (a) Major tectonic features and the distribution of four active faults. Polygon colors denote individual known fault systems. (b) Aftershock distributions of EQ2018 and EQ2024. For the EQ2024 sequence, the spatial patterns differ between T1 (Days 0–18) and T2 (Days 19–30).

https://doi.org/10.5194/egusphere-2026-3012
Preprint. Discussion started: 16 June 2026

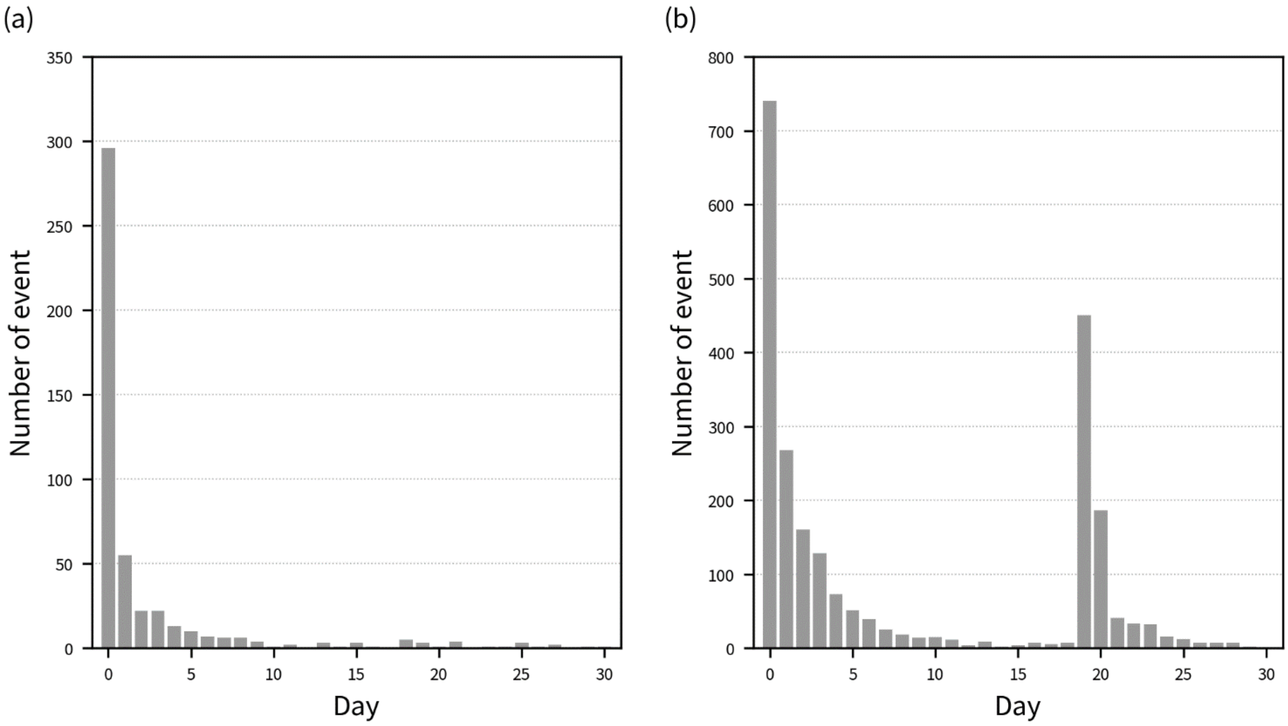

Figure 2: Daily aftershock counts ($M_L \geq 3$) within 30 days following the mainshock. (a) Aftershock sequence of EQ2018; (b) Aftershock sequence of EQ2024.

3 Methodology

Two unsupervised machine learning techniques were employed to analyze earthquake sequences, with the objective of delineating potential fault planes beyond those directly associated with the mainshock rupture. First, the Density-Based Spatial Clustering of Applications with Noise (DBSCAN) algorithm was applied to classify seismic events into clusters, thereby grouping earthquakes according to their spatial proximity. This clustering step facilitates the identification of coherent seismic substructures that may correspond to distinct rupture zones. Second, Principal Component Analysis (PCA) was utilized to delineate potential fault structures by extracting dominant spatial orientations from the clustered data. Finally, the maximum likelihood of earthquake magnitude for each fault rupture was evaluated using an empirical equation, providing quantitative constraints on the seismogenic potential of the identified structures.

3.1 Clustering the seismic sequence

The DBSCAN algorithm is based on data density, capable of partitioning two-dimensional or three-dimensional spatial datasets while automatically identifying noise points (Ester et al., 1996). DBSCAN relies on two key parameters: ε, which defines the neighborhood search radius, and *MinPts*, which specifies the minimum number of points required to form a cluster. The neighborhood of a point p in DBSCAN is defined as:

$$N_\varepsilon(p) = \{q \in D | dist(p, q) \leq \varepsilon\}$$

where D denotes the dataset (seismic locations), ε is the neighborhood radius, and $dist(p, q)$ is the distance between points p and q.

Based on these parameters, DBSCAN classifies points into three categories: (i) core points, which contain at least *MinPts* neighbors within the ε-radius; (ii) border points, which have fewer than *MinPts* neighbors but lie within the neighborhood of a core point; and (iii) noise points, which are neither core nor border points. Clustering proceeds iteratively from unclassified core points, aggregating all density-reachable points into a cluster. Each cluster must contain at least one core point, and closure under reachability ensures that any point density-reachable from a cluster member is also included in that cluster. Data points that do not belong to any cluster are classified as noise (Ester et al., 1996; Schubert et al., 2017; Hahsler et al., 2019). To mitigate the influence of spatial anisotropy in earthquake sequences—commonly observed as horizontal extensions exceeding vertical ones (Piegari et al., 2022)—we applied Min-Max scaling normalization prior to clustering. This preprocessing step ensures that differences in spatial variance do not bias the clustering outcome, thereby improving the robustness of DBSCAN in delineating potential rupture structures.

3.2 Identifying the fault geometry

Following clustering, Principal Component Analysis (PCA) was utilized to extract the geometric characteristics of the rupture planes. PCA is a linear statistical technique that enables dimensionality reduction of complex, high-dimensional datasets while preserving their dominant features and characterizing the geometric properties of clustered seismicity. This approach systematically decomposes a dataset D (seismic locations), typically through singular value decomposition (SVD**)** or eigenvalue decomposition, to identify principal components (PC) that capture the dominant variance structure (Pearson, 1901). The covariance matrix of D is computed, and its eigenvectors define orthogonal directions of maximum variance, while the corresponding eigenvalues quantify the magnitude of variance along each direction.

For dimensionality reduction, the dataset is projected onto the first k principal components associated with the largest eigenvalues, thereby retaining the most significant features while suppressing noise and redundancy. In the case of three-dimensional earthquake distributions, PCA yields three eigenvalues ($\lambda_1, \lambda_2, \lambda_3$). When λ_1 and λ_2 are substantially greater than λ_3, the seismicity exhibits a planar structure, consistent with fault-plane geometry. Conversely, when the eigenvalue ratio approaches 1:1:1, the distribution lacks a dominant orientation, indicating isotropy or the absence of a well-defined structural pattern.

To establish the geometric characteristics of the planes, this study employs the eigenvectors of PC1 and PC2 to construct PCA-derived surfaces, which are treated as potential fault structures. The third principal component (PC3) is adopted as the normal vector to calculate the strike and dip of the PCA planes (Quinn and Ehlmann, 2019). The computational procedure involves projecting earthquake hypocenter locations onto a new coordinate system defined by PC1 and PC2, from which the geometric centroid ($\bar{P}$) is determined. The maximum and minimum values along the principal component directions are then used to delineate the boundaries of the fitted plane, thereby constraining its spatial extent.

The parametric equation of the plane is expressed as:

$$P(u, v) = \bar{P} + u \cdot PC1 + v \cdot PC2$$

where $\bar{P}$ represents the centroid of the data points, and u and v denote the coordinate parameter ranges along the first and second principal component axes, respectively. This formulation not only provides a simplified representation of the dominant spatial trend within each cluster but also serves as a quantitative basis for comparing cluster-derived fault geometries with known tectonic structures. While the PCA-derived planes cannot fully capture complex curvatures or non-linear fault morphologies, they offer a robust first-order approximation of potential rupture surfaces, thereby contributing to the identification of latent fault systems and guiding subsequent structural interpretations. Beyond its immediate application to rupture plane delineation, this approach also contributes to broader seismic hazard assessment, as it facilitates the recognition of previously unmapped or secondary fault systems that may influence future seismic activity.

3.3 Evaluating the potential magnitude

Seismological studies have consistently demonstrated that earthquake magnitude is closely related to fault-plane parameters such as length, width, and overall rupture area (Wells and Coppersmith, 1994; Huang and Wang, 2002; Huang and Wang, 2009; Leonard, 2010; Stirling et al., 2013). These empirical scaling laws have been widely adopted in seismic hazard assessment because they provide a practical means of linking observed or inferred fault geometries with realistic magnitude scenarios.

Building on this foundation, Wells and Coppersmith (1994) developed regression-based formulas that quantitatively link fault geometry to earthquake magnitude. In the present study, we apply their empirical equation to estimate the maximum seismic moment magnitude (M_w) associated with rupture planes delineated through PCA. The formula is expressed as:

$$M_w = 4.07 + 0.98 \times Area$$

where *Area* denotes the surface area of the PCA-derived rupture plane, measured in square kilometers. This provides a systematic means of translating geometric properties inferred from seismic clustering and PCA into estimates of potential earthquake size.

https://doi.org/10.5194/egusphere-2026-3012
Preprint. Discussion started: 16 June 2026

Beyond its methodological utility, this integration of PCA-based rupture delineation with established magnitude–area relationships enhances the reliability of earthquake sequence analysis. It also contributes to a more comprehensive understanding of seismic potential in tectonically active regions. Importantly, such an approach strengthens the connection between data-driven structural characterization and hazard assessment, offering insights that are valuable not only for advancing scientific research but also for informing disaster-prevention strategies and policy planning.

4 Results

As illustrated in Figure 1, the spatial distributions of the two earthquake sequences exhibit markedly different patterns. The hypocenters of EQ2018 are concentrated at depths of 3–20 km, whereas those of EQ2024 are distributed across 1–45 km. Beyond delineating the nearby fault structures, this analysis also enables the identification of rupture mechanisms associated with the structures triggered by the respective mainshocks. In particular, the clustering and geometric characterization of seismicity provide insights into whether the mainshock activated adjacent or secondary fault segments, thereby revealing the complexity of rupture propagation. Such spatial analyses are critical for understanding the interplay between primary rupture planes and subsidiary structures, as they highlight how earthquake sequences may evolve differently depending on local fault geometry and stress conditions.

4.1 Earthquake clustering

To mitigate the pronounced spatial anisotropy observed in both cases, Min-Max scaling was first applied to normalize longitude, latitude, and depth values to the range [0, 1], followed by DBSCAN clustering. The parameter settings included *MinPts* in the range [10, 12] and ε searched within [0, 1]. Clustering validity was evaluated using the Silhouette Score (*SS*; Bariklana and Fauzan, 2023), which ranges from [-1, 1]. An $SS < 0$ indicates misclassification of data, whereas values approaching 1 signify improved clustering performance (Rousseeuw et al., 1987).

This methodological framework ensures that clustering results are not biased by differences in spatial scale between horizontal and vertical coordinates. By combining normalization with DBSCAN's density-based approach, the analysis is able to capture coherent seismic substructures while minimizing distortions caused by depth variability. The use of the Silhouette Score further provides a quantitative benchmark for assessing the robustness of clustering outcomes, thereby enhancing confidence in the identification of potential rupture zones.

Figure 3 presents the clustering analysis results for EQ2018. In Figure 3a, although the parameters $\varepsilon = 0.08$ and $MinPts = 12$ yielded the maximum *SS*, the spatial distribution of clusters failed to align with known geological structures. To prioritize structural accuracy, the second-best performing configuration ($\varepsilon = 0.07$, $MinPts = 10$) was adopted, as it provided a more physically representative clustering mode. Under this configuration, approximately 12.4% of events were classified as noise, while the remaining events were grouped into four clusters (A0–A3; Figure 3b).

Cluster A0 exhibits a northeast–southwest orientation, includes the mainshock, and accounts for 66.6% of the events. Cluster A1 is located offshore, with aftershocks distributed along a northeast–east to southwest–west trend, comprising 8.8% of the events. Clusters A2 and A3 are situated northeast of A0, representing 4.7% and 7.5% of the events, respectively.

Figures 3c–f illustrates the depth statistics of each cluster. Cluster A0, which includes the mainshock (M_L = 6.26; M_w = 6.37), exhibits hypocenters with a mean depth of 9 km. Cluster A1 has a mean depth of 6 km, with maximum magnitudes of M_L^{max} = 5.52 ($M_w^{\max}$ = 5.36). Cluster A2 is characterized by a mean depth of 12 km, and M_L^{max} = 4.51 ($M_w^{\max}$ = 4.29). Cluster A3 shows a mean depth of 13 km, and M_L^{max} = 4.37 ($M_w^{\max}$ = 4.16).

This clustering analysis highlights the importance of balancing statistical performance with geological plausibility. While the highest *SS* value indicated optimal mathematical separation, the adopted configuration better reflects the underlying tectonic framework. Such an approach ensures that clustering outcomes are not only statistically valid but also geologically meaningful, thereby strengthening the interpretation of aftershock sequences in relation to potential rupture zones.

Figure 4 presents the clustering analysis results for EQ2024. Using the parameter combination that yielded the maximum *SS*, with ε = 0.07 and *MinPts* = 10 (Figure 4a), approximately 6.5% of events were classified as noise, while the remaining events were grouped into five clusters (B0–B4; Figure 4b). Clusters B0, B3, and B4 exhibit a northeast–southwest orientation, accounting for 35.3%, 19.7%, and 36.5% of aftershocks, respectively. Cluster B1 shows a northwest–southeast orientation (1%), while Cluster B2 is located offshore, with aftershocks distributed along a west-northwest to east-southeast trend (1%).

Figures 4c–f present histograms of earthquake depth and event counts across two time intervals. During the first interval (gray bars), aftershocks were predominantly concentrated in Clusters B3 and B4, which collectively accounted for 85% of the total events, with Cluster B4 exhibiting the highest seismicity during this initial stage. In contrast, during the second interval (red bars), 89% of the aftershocks were classified within Cluster B0, leaving only a minor fraction of events in Clusters B3 and B4. Depth distribution analysis further reveals that seismic activity in Cluster B0 during this later phase was highly concentrated at depths shallower than 15 km, with the highest density observed between 7 and 9 km.

Considering the entire observation period, the spatial and statistical characteristics of each cluster are summarized as follows: Cluster B0, which includes the mainshock (M_L = 7.19; M_w = 7.3), exhibits hypocenters with a mean depth of 9 km. Cluster B1 shows a deeper depth range with a mean depth of 29 km and $M_L^{\max}$ = 5.2 ($M_w^{\max}$ = 4.46). Cluster B2 is characterized by a mean depth of 18 km and $M_L^{\max}$ = 5.98 ($M_w^{\max}$ = 5.71). Cluster B3 displays the greatest depth range, with a mean depth of 31 km and $M_L^{\max}$ = 6.31 ($M_w^{\max}$ = 5.63). Cluster B4 exhibits a mean depth of 15 km and $M_L^{\max}$ = 6.56 ($M_w^{\max}$ = 6.64).

This analysis underscores the temporal migration of seismicity from deeper clusters (B3 and B4) during the early stage to the shallower Cluster B0 in the later stage. Such evolution suggests a progressive redistribution of stress, with initial rupture activity concentrated at depth before shifting upward to shallower crustal levels. The observed clustering patterns therefore provide important insights into rupture propagation dynamics and highlight the heterogeneous nature of fault activation during the EQ2024 sequence.

https://doi.org/10.5194/egusphere-2026-3012
Preprint. Discussion started: 16 June 2026

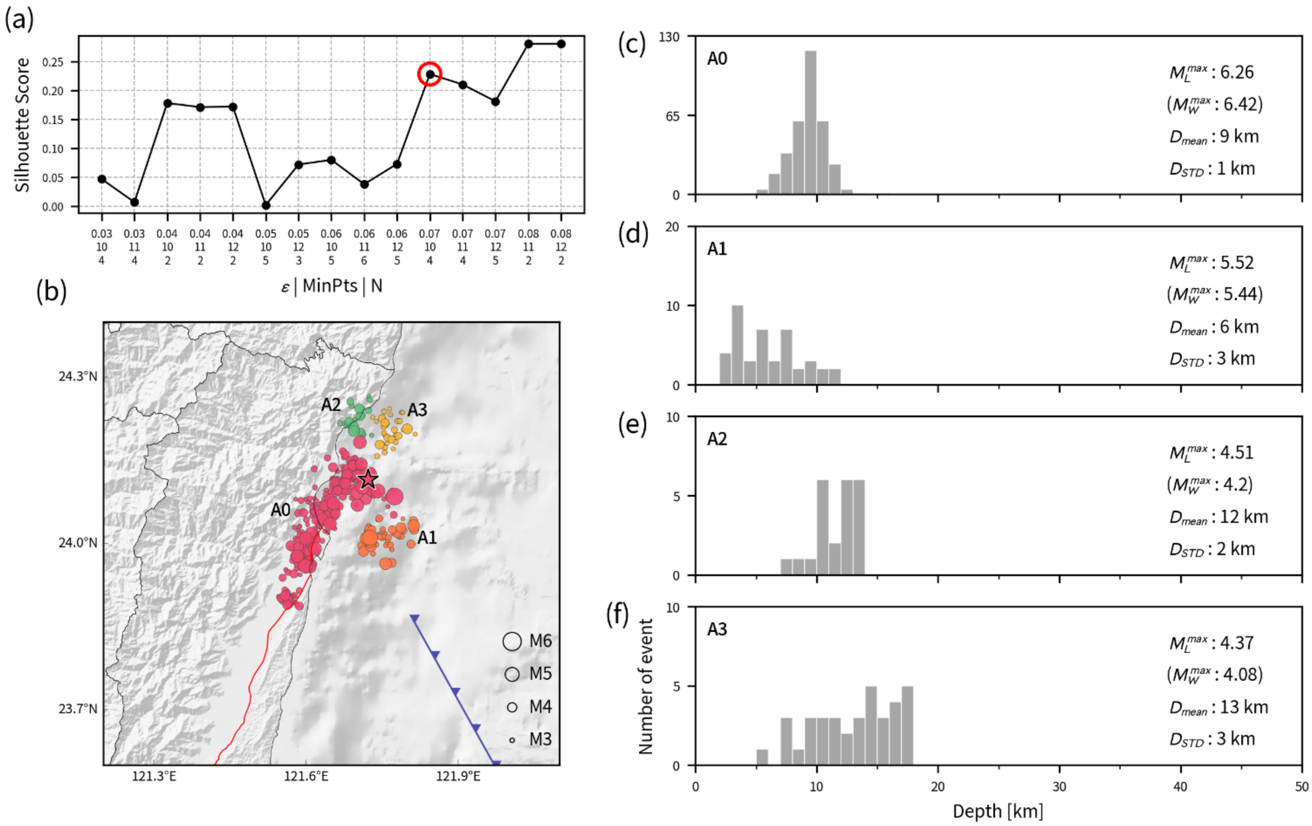

Figure 3. (a) Clustering results for EQ2018 using the parameter combination that yielded the maximum Silhouette Score. (b) Spatial distribution of clustered earthquakes. (c–f) Depth statistics of clustered earthquakes.

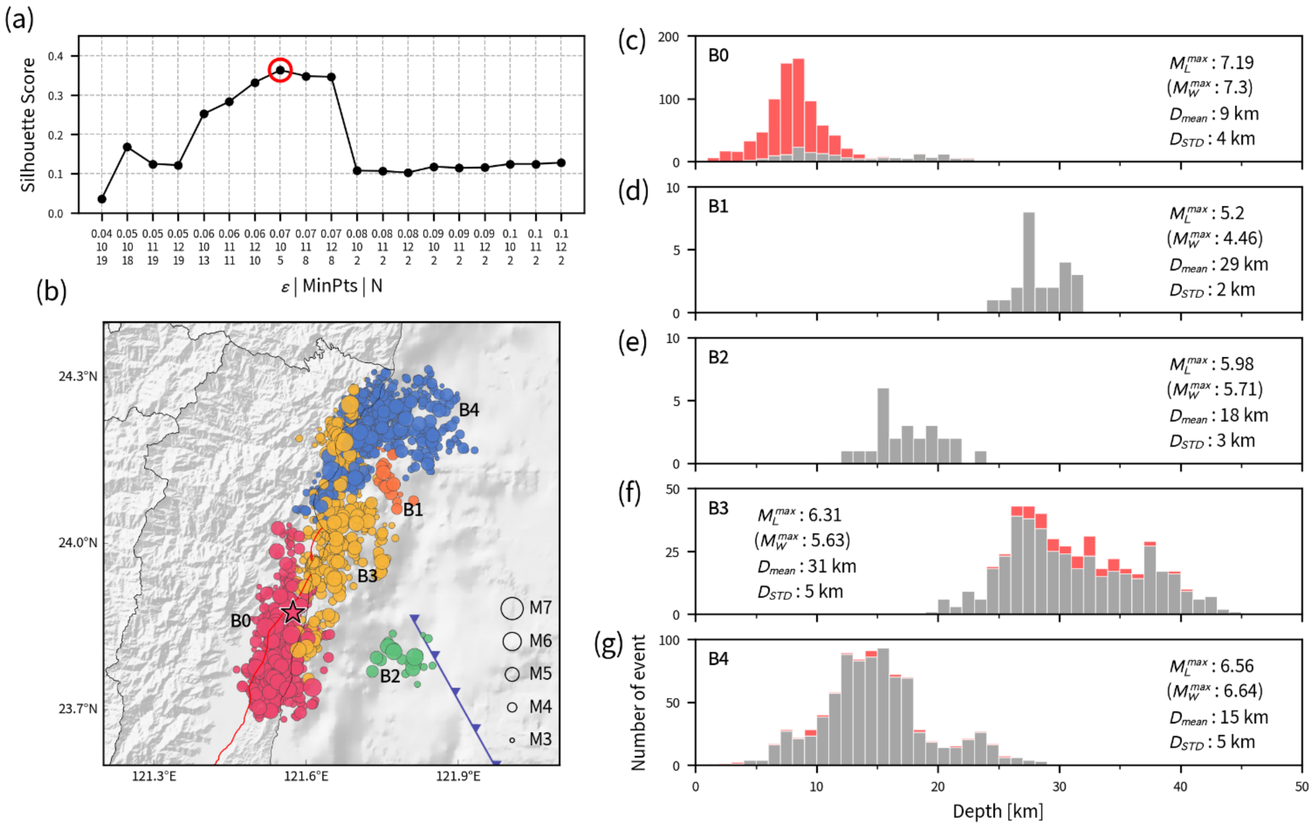

Figure 4. (a) Clustering results for EQ2024 obtained using the parameter combination that produced the maximum Silhouette Score. (b) Spatial distribution of clustered earthquakes. (c–g) Depth statistics of clustered earthquakes. The gray bars indicate the first interval, while the red bars indicate the second interval.

290 4.2 Identification of potential fault structures

Three-dimensional spatial analysis reveals distinct distributional trends in hypocenter locations. To further characterize these patterns, Principal Component Analysis (PCA) was employed. Figure 5 illustrates the fitting result using the aftershock distribution of Cluster A0 as a representative example. To ensure balanced weighting across all spatial dimensions, the coordinates were pre-processed with Min-Max scaling normalization prior to fitting based on PC1 and PC2. The best-fit plane was centered at the geometric centroid of the cluster hypocenters, ensuring that the derived structure reflects the mean spatial trend of the seismic sequence.

As shown in the multi-angle views of the fault plane, the first and second principal component vectors (PC1 and PC2) represent the axes of maximum spatial variance, characterizing the aspect ratio and lateral extent of the fault plane. The orientation of the plane is uniquely determined by the normal vector PC3. Through a coordinate transformation of PC3, the strike and dip angles for the cluster were determined, effectively converting the discrete hypocentral distribution into a geologically meaningful fault segment.

Subsequently, the derived plane geometry was used to estimate rupture area and calculate the potential maximum seismic moment magnitude ($M_w^{\max}$). This stepwise workflow—normalization, PCA fitting, orientation extraction, and magnitude estimation—demonstrates how statistical methods can be integrated with geological interpretation. By bridging three-dimensional clustering with fault-plane characterization, this approach enhances the reliability of rupture analysis and provides quantitative insights into the seismogenic potential of tectonically active regions.

For EQ2018, as show in Figure 6a, the earthquake sequence can be divided into four clusters (A0–A3), all with hypocenter depths shallower than 20 km. The optimized PCA-derived fault planes are denoted as P_{A0}, P_{A1}, P_{A2}, and P_{A3}.

All four planes exhibit northeast–southwest orientations and dip westward, with P_{A0} and P_{A1} characterized by steeper dips (62.5° and 69.9°, respectively), while P_{A2} and P_{A3} show more moderate inclinations (51.4° and 58.1°, respectively).

The detailed orientations and estimated maximum magnitudes are as follows:

- P_{A0}: strike = 226.6°, dip = 62.5°, $M_w^{\max}$ = 6.70
- P_{A1}: strike = 234.2°, dip = 69.9°, $M_w^{\max}$ = 6.11
- P_{A2}: strike = 194.1°, dip = 51.4°, $M_w^{\max}$ = 5.84
- P_{A3}: strike = 209.2°, dip = 58.1°, $M_w^{\max}$ = 6.06

The centroid moment tensor (CMT) solutions of the largest-magnitude events within each cluster, as determined by AutoBATS (Jian et al., 2018; https://tecdc.earth.sinica.edu.tw/FM/AutoBATS/; last accessed 13 January 2026), further corroborate the PCA-derived fault geometries. This consistency underscores the reliability of the combined clustering–PCA framework in capturing the dominant rupture orientations and structural controls of the EQ2018 sequence.

These results indicate that the EQ2018 ruptures were predominantly confined to shallow crustal levels, with clustering orientations reflecting localized structural controls. The coexistence of northeast–southwest and northwest–southeast fault orientations suggests that multiple interacting fault segments were activated during the sequence. This interplay highlights the structural complexity of the region and underscores the importance of integrating spatial clustering with PCA-based fault-plane analysis to capture the heterogeneity of rupture processes.

In contrast to EQ2018, the hypocenter depth distributions of EQ2024 clusters vary more substantially, extending to greater depths. As shown in Figure 6b, the sequence can be divided into five clusters (B0–B4), with optimized PCA planes designated as P_{B0}, P_{B1}, P_{B2}, P_{B3}, and P_{B4}. Based on strike and dip orientations, these planes can be categorized into three groups:

- Northeast–southwest striking, west-dipping planes: P_{B0} (strike = 210.1°, dip = 85.8°, $M_w^{\max}$ = 6.99) and P_{B2} (strike = 198.5°, dip = 41.0°, $M_w^{\max}$ = 6.13).
- Northeast–southwest striking, southeast-dipping planes: P_{B3} (strike = 41.7°, dip = 85.2°, $M_w^{\max}$ = 7.19) and P_{B4} (strike = 35.3°, dip = 60.1°, $M_w^{\max}$ = 7.06).
- East-West striking, north-dipping plane: P_{B1} (strike = 276.3°, dip = 47.6°, $M_w^{\max}$ = 5.88).

Compared with EQ2018, the clustering of EQ2024 reveals a more complex rupture geometry, involving both shallow and deeper hypocenters as well as multiple dipping directions. This diversity in fault orientations underscores the structural 335 heterogeneity of the seismogenic zone and suggests that EQ2024 ruptures may have engaged a broader range of fault segments. The coexistence of steeply dipping and moderately inclined planes, combined with varying depth distributions, highlights the dynamic nature of rupture propagation and points to a more intricate stress redistribution process during the EQ2024 sequence.

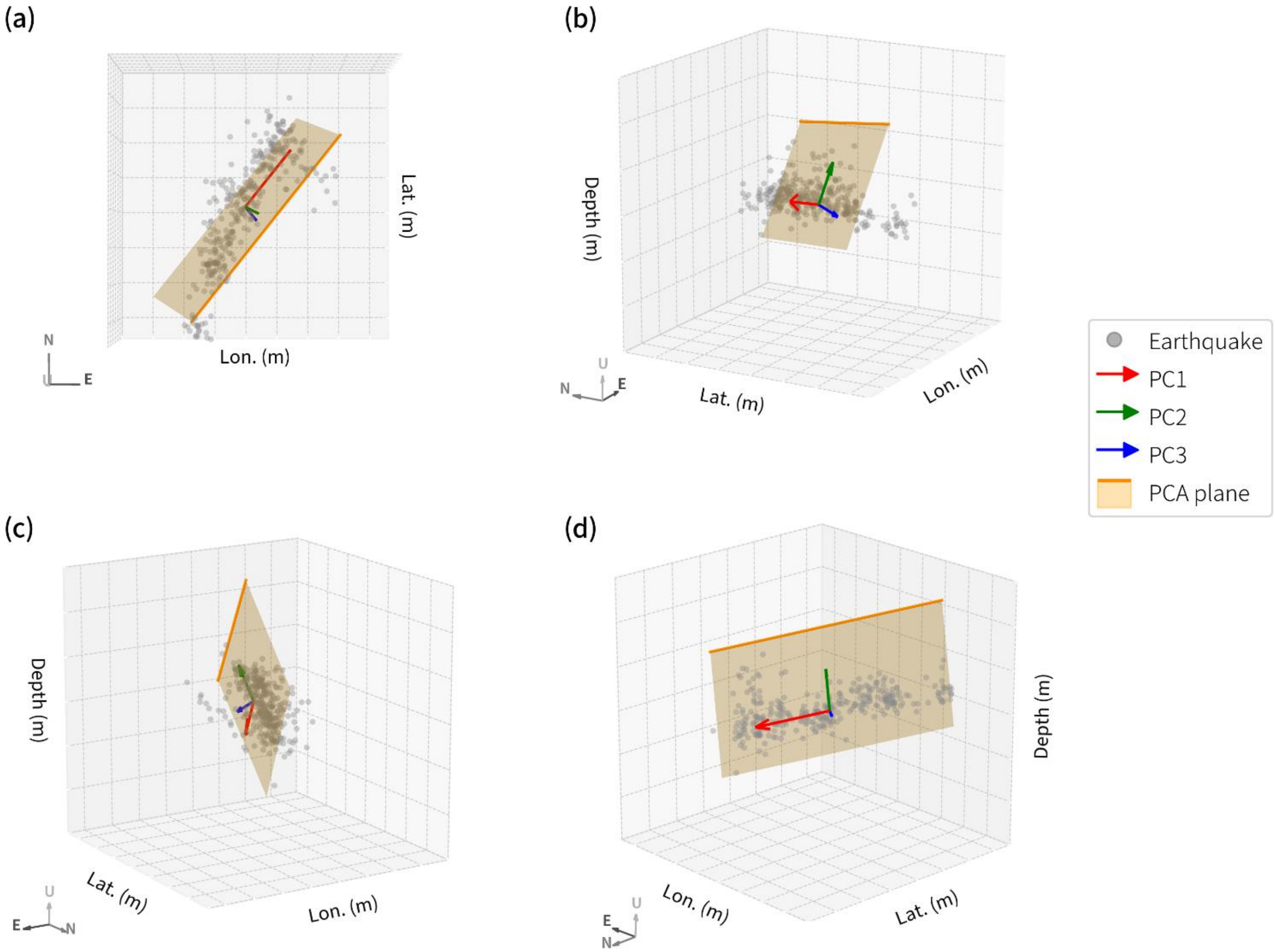

340 **Figure 5. Fault geometry construction using PCA. Multi-angle views demonstrate the alignment between the hypocentral distribution (circles) and the fitted plane (rectangle). Red, green, and blue arrows correspond to PC1, PC2, and the normal vector PC3.**

https://doi.org/10.5194/egusphere-2026-3012
Preprint. Discussion started: 16 June 2026

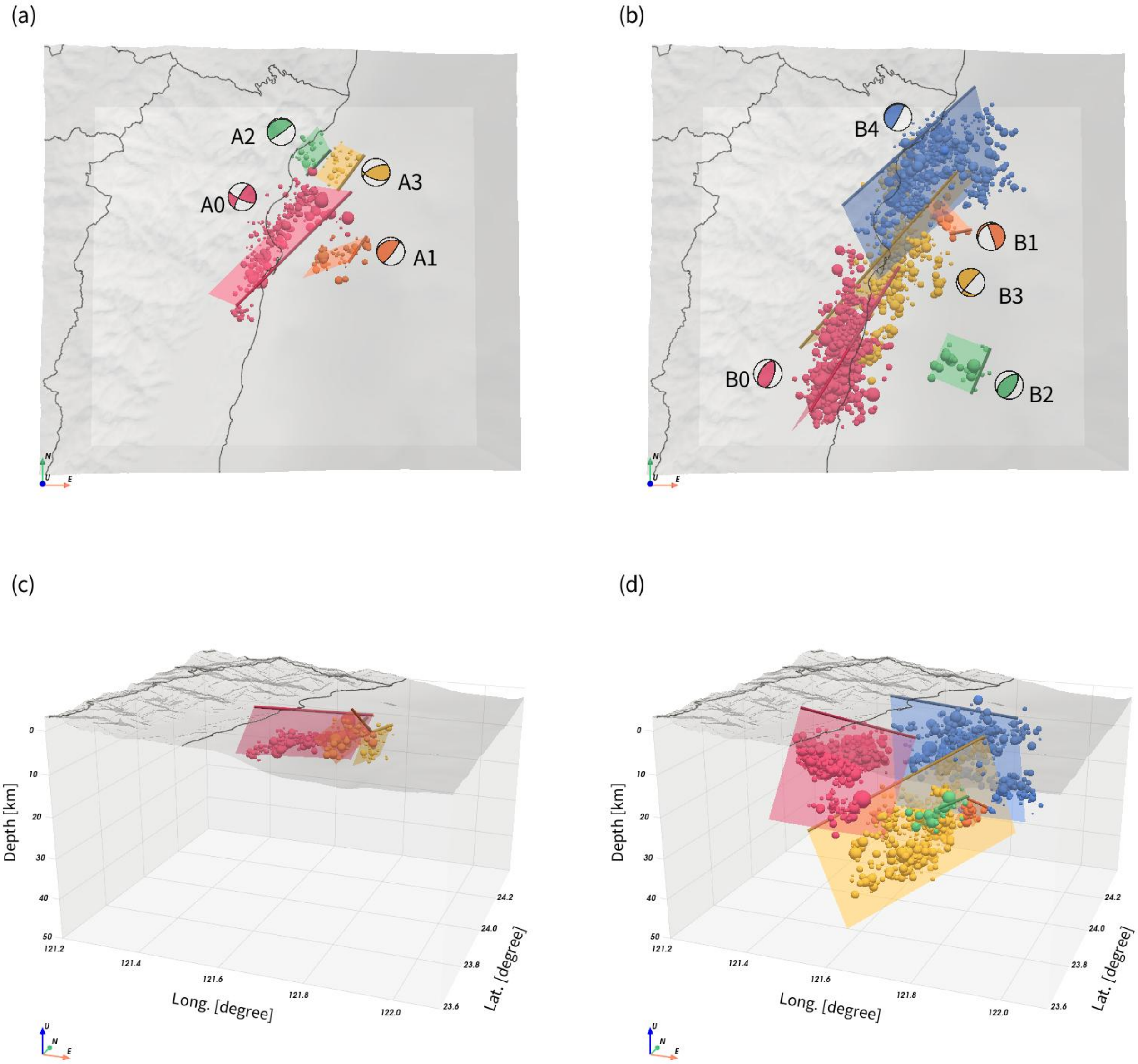

Figure 6. PCA-derived planes of clustered earthquakes. (a, c) EQ2018 sequence, divided into four clusters (A0–A3) in top and side views (b, d) EQ2024 sequence, divided into five clusters (B0–B4) in top and side views. Rectangles represent PCA planes, colors denote individual clusters, and lines indicate the near-surface boundary. Focal mechanisms represent the largest magnitude event within each cluster.

https://doi.org/10.5194/egusphere-2026-3012
Preprint. Discussion started: 16 June 2026

4.3 Comparison with known fault systems

This study employs three-dimensional visualization techniques to investigate the relationship between the clustering of EQ2018 and EQ2024 and four known active faults (Chen et al., 2024), as well as other potentially triggered, unidentified structures. This approach is particularly valuable in cases where earthquake sequences do not follow a single orientation or occur in structurally complex regions, where conventional two-dimensional cross-sections alone are insufficient to capture spatial continuity and tectonic associations.

By integrating clustering results with three-dimensional fault geometries, the method provides a more comprehensive perspective on rupture processes and their relation to regional tectonics. In addition, three-dimensional visualization facilitates the identification of subtle geometric patterns—such as overlapping fault segments, depth-dependent variations, and multi-directional rupture propagation—that may otherwise remain obscured in traditional analyses. This integration strengthens the interpretive framework for seismic sequence analysis and enhances the reliability of linking observed aftershock distributions to both mapped and unmapped fault systems.

Figure 6a and 6c shows the three-dimensional spatial distribution of EQ2018 clusters. The mainshock of P_{A0} is located near the Milun Fault, while the remaining events are concentrated beneath the mainshock, exhibiting a west-dipping trend. Most events are geometrically consistent with the CRF model, though a small number are located near the Milun and Lingding Faults. The other three clusters are situated offshore: P_{A1} and P_{A3} lie east of the CRF, while P_{A2} is located west of the CRF; however, these clusters cannot be correlated with existing active fault models. This suggests that, in addition to ruptures along mapped structures, EQ2018 may have involved activity on unmapped or subsidiary faults in offshore regions.

This finding aligns with previous studies that identified the 2018 Hualien earthquake as a complex multi-fault rupture event (Tung et al., 2019; Lo et al., 2019; Huang and Huang, 2018; Wen et al., 2019; Huang and Wang, 2022). The rupture initiated along the steep, west-dipping CRF at depth and subsequently activated the east-dipping Milun Fault. Although the A1, A2, and A3 clusters did not occur directly on the CRF, the spatial orientation of their planes shows geometric similarity to the CRF model, with all PCA-derived planes dipping westward. Furthermore, the dip angles of these three clusters are gentler than that of P_{A0}, suggesting that they may have been triggered by stress perturbations associated with the mainshock, thereby activating minor structures in the vicinity of the CRF.

Figure 6b and 6d presents the three-dimensional spatial distribution of EQ2024 clusters. The mainshock of P_{B0} is located on the Lingding Fault. Hypocenter distribution indicates that P_{B0} events are concentrated in the shallow region (<15 km) between the Lingding and Central Range Faults, while deeper events (>15 km) are almost entirely aligned along the Lingding Fault. P_{B3} events are concentrated in the deeper region (≥20 km); in the southern sector (latitude <23.95°), hypocenters align with the Lingding Fault, whereas northern events cannot be matched to existing fault models, implying possible activation of previously unrecognized structures. P_{B4} exhibits a distinctive spatial pattern: on land, hypocenters display a northeast–southwest orientation along CRF, while events at latitudes 24.1°–24.3° extend eastward offshore, with depths reaching up to

28 km. This offshore extension highlights the complex interplay between onshore and offshore fault systems and suggests that EQ2024 ruptures may have propagated across multiple fault segments with varying orientations and depths.

P_{B0} exhibits a steep west-dipping orientation due to the spatial distribution of hypocenters shifting westward from the deep, east-dipping LVF to the shallower CRF system. This apparent geometry suggests that P_{B0} physically captures the stress triggering between the deep LVF and the shallower CRF system, dynamically linking these two oppositely dipping structures during the seismic sequence.

P_{B3}, in contrast, is characterized by a steep east-dipping fault plane, displaying structural features that differ markedly from those of the Lingding Fault to the south, thereby indicating localized variations in fault kinematics and stress regime. P_{B4} also dips eastward, and its geometry is closely associated with the tectonic transition zone located at the northern end of Hualien, where the tectonic setting evolves from plate collision to subduction. This transition zone encompasses key geodynamic features such as the Ryukyu Trench, the accretionary prism, and the forearc basin, which together mark the boundary between collisional and subduction processes (Font et al., 2001; Shyu et al., 2005; Wu et al., 2009; Lo et al., 2019; Yen et al., 2019; Chen et al., 2024). The presence of P_{B4} within this transitional framework highlights the role of regional-scale tectonics in shaping local fault geometries and suggests that the observed eastward dips may reflect the progressive accommodation of compressional stresses as they transition into subduction-related deformation.

5 Discussion

In this study, we establish a framework that integrates two unsupervised learning approaches to identify potential fault structures from earthquake sequences. First, the DBSCAN algorithm is applied to partition seismic events into clusters, with the Silhouette Score serving as the principal metric for cluster validation. Second, Principal Component Analysis (PCA) is employed to extract the geometric characteristics of fault planes, utilizing the leading three principal components to define their orientation and spatial extent.

The PCA-derived planes are consistent with the fault-plane solutions of the largest-magnitude events within each cluster. This consistency highlights the robustness of the framework, demonstrating that statistical clustering combined with PCA can effectively translate complex seismic distributions into geologically meaningful fault structures. By bridging unsupervised learning with seismological interpretation, the approach provides a systematic means of detecting both mapped and potentially unmapped rupture geometries, thereby enhancing the reliability of earthquake sequence analysis and contributing to improved seismic hazard assessment.

Apart from the mainshock cluster, which is located along a known tectonic structure, the remaining clusters reveal fault-plane orientations that cannot be directly linked to established faults. This outcome provides supplementary insights into the existence of previously unrecognized or latent fault structures. Such findings highlight the utility of combining clustering and

https://doi.org/10.5194/egusphere-2026-3012
Preprint. Discussion started: 16 June 2026

PCA in delineating subtle fault geometries, thereby contributing to a more comprehensive understanding of regional seismotectonic frameworks.

The limitations and potential applications of the proposed workflow can be summarized as follows. By testing multiple parameter sets for clustering and evaluating the Silhouette Score, the parameter combination yielding the maximum *SS* value (ε and *MinPts*) is prioritized as the final clustering criterion. This automated procedure enables systematic grouping of aftershock sequences and subsequent computation of PCA-derived planes. Nevertheless, manual verification remains essential to ensure consistency between clustering results and known geological structures. If discrepancies arise, the parameters associated with the second-highest *SS* value are adopted, and the clustering–PCA analysis is repeated.

It should also be noted that PCA analysis can only represent the dominant planar trend of the spatial distribution within each cluster. Fault geometries exhibiting pronounced curvature or arc-shaped features cannot yet be effectively fitted or fully characterized. This limitation underscores the need for complementary approaches—such as advanced surface-fitting techniques or geophysical imaging—to capture more complex rupture geometries.

Beyond geometric delineation, the PCA-derived planes provide a quantitative basis for assessing seismic potential. By utilizing the calculated area of each fitted plane, we can estimate the potential maximum moment magnitude for each cluster. Comparing these estimated values with the observed mainshock magnitudes allows for an evaluation of rupture completeness and stress release patterns. Such calculations are instrumental in identifying the hazard potential of blind faults or offshore structures that lack surface expressions.

Regarding data limitations, aftershock numbers naturally decay over time following a major earthquake. A complete aftershock catalog requires sufficient observational duration and data processing. Consequently, in the early post-seismic stage, this method can only provide preliminary insights into the relationship between aftershock clustering and regional tectonics, serving as a reference for rapid structural interpretation and assessment. Detailed analyses of the main rupture geometry must await the establishment of a more comprehensive earthquake catalog.

Despite these constraints, the results of this study demonstrate that when earthquake events exhibit a clear linear spatial distribution, PCA analysis can effectively identify the geometric characteristics of rupture planes. In cases where earthquake numbers are large and distributions are more complex, the fitted PCA planes may not perfectly match the seismicity patterns. However, they still provide valuable indications of the potential location and scale of rupture surfaces, thereby offering a useful tool for identifying latent fault structures and guiding subsequent tectonic interpretations.

6 Conclusions

This study establishes a robust framework that integrates unsupervised learning and three-dimensional visualization to identify potential fault structures from earthquake sequences. By combining DBSCAN clustering with Silhouette Score validation and PCA-derived fault-plane analysis, the approach effectively translates complex hypocenter distributions into geologically meaningful rupture geometries. Application to the EQ2018 and EQ2024 sequences demonstrates the framework's ability to capture both mapped and previously unrecognized fault orientations, revealing shallow west-dipping ruptures in EQ2018 and more complex, multi-directional, and deeper ruptures in EQ2024.

Three-dimensional visualization further highlights the interplay between known active faults and latent structures, underscoring the structural heterogeneity of the seismogenic zone and the influence of tectonic transition processes. While PCA provides reliable characterization of dominant planar trends, limitations remain in representing curved or irregular geometries, pointing to the need for complementary methods in future work. Overall, the proposed workflow enhances seismotectonic interpretation, offers new insights into rupture propagation across complex fault systems, and contributes to improved seismic hazard assessment in tectonically active regions.

Code and data availability

The datasets used and analysed during the current study available from the corresponding author on reasonable request.

Author contributions

KTT: Writing draft, calculations, visualization; MWH, SSK: review, editing; all authors participated in discussions and approved the final manuscript.

Competing interests

The authors declare no competing interests.

Acknowledgements

The authors gratefully acknowledge the Central Weather Administration of Taiwan for providing high-quality earthquake data. Appreciation is also extended to the editor and anonymous reviewers for their constructive comments and valuable suggestions, which have greatly improved the quality of this article.

Financial support

This work was supported by National Science and Technology Council (Grant No. NSTC 114-2124-M-865-001). The financial contributions are gratefully acknowledged.

References

Ankerst, M., Breunig, M. M., Kriegel, H. P., and Sander, J.: OPTICS: Ordering points to identify the clustering structure. ACM Sigmod Record, 28, 49–60, https://doi.org/10.1145/304181.304187, 1999.

Bariklana, M. and Fauzan, A.: Implementation of the dbscan method for cluster mapping of earthquake spread location, BAREKENG: J. Math. & App., 17, 0867–0878, https://doi.org/10.30598/barekengvol17iss2pp0867-0878, 2023.

Central Weather Administration (CWA, Taiwan): Central Weather Administration Seismographic Network [Data set], International Federation of Digital Seismograph Networks, https://doi.org/10.7914/SN/T5, 2012.

Chen, W. S., Yen, I. C., Fengler, K. P., Rubin, C. M., Yang, C. C., Yang, H. C., Chang, H. C., Lin, C. W., Lin W. H., Liu, Y. C., and Lin, Y. H.: Late Holocene paleoearthquake activity in the middle part of the Longitudinal Valley fault, eastern Taiwan, Earth Planet. Sci. Lett., 264, 420–437, https://doi.org/10.1016/j.epsl.2007.09.043, 2007.

Chen, W. S., Wu, Y. M., Yeh, P. Y., Lai, Y. X., Ke, S. S., Ke, M. C., and Yang, C. Y.: Insights into the seismogenic structures of the arc-continent convergent plate boundary in eastern Taiwan, Terr. Atmos. Ocean. Sci., 35, 13, https://doi.org/10.1007/s44195-024-00065-7, 2024.

Cheng, C. T., Hsieh, P. S., Lin, P. S., Yen, Y. T., and Chan, C. H.: Probability seismic hazard mapping of Taiwan, Encyclopedia of earthquake engineering, 1997–2020, https://doi.org/10.1007/978-3-642-35344-4_100, 2015.

Chuang, R. Y., Johnson, K. M., Kuo, Y. T., Wu, Y. M., Chang, C. H., and Kuo, L. C.: Active back thrust in the eastern Taiwan suture revealed by the 2013 Rueisuei earthquake: evidence for a doubly vergent orogenic wedge?, Geophys. Res. Lett., 41, 3464–3470, https://doi.org/10.1002/2014GL060097, 2014.

Ester, M., Kriegel, H. P., Sander, J., and Xu, X.: A density-based algorithm for discovering clusters in large spatial databases with noise, in: Proceedings of the Second International Conference on Knowledge Discovery and Data Mining, 226–231, 1996.

Fan, Z. and Xu, X.: Application and visualization of typical clustering algorithms in seismic data analysis, Procedia Comput. Sci., 151, 171–178, https://doi.org/10.1016/j.procs.2019.04.026, 2019.

Font, Y., Liu, C. S., Schnurle, P., and Lallemand, S.: Constraints on backstop geometry of the southwest Ryukyu subduction based on reflection seismic data, Tectonophysics, 333, 135–158, https://doi.org/10.1016/S0040-1951(00)00272-9, 2001.

Freed, A. M.: Earthquake triggering by static, dynamic, and postseismic stress transfer, Annu. Rev. Earth Planet. Sci., 33, 335-367, https://doi.org/10.1146/annurev.earth.33.092203.122505, 2005.

Hahsler, M., Piekenbrock, M., and Doran, D.: dbscan: Fast density-based clustering with R, J. Stat. Soft., 91, 1–30, https://doi.org/10.18637/jss.v091.i01, 2019.

Herrmann, M., Piegari, E., and Marzocchi, W.: Revealing the spatiotemporal complexity of the magnitude distribution and b-value during an earthquake sequence, Nat. Commun., 13, 5087, https://doi.org/10.1038/s41467-022-32755-6, 2022.

Hsu, T. L.: Geology of the coastal range, eastern Taiwan, Bull. Centr. Geol. Surv., 8, 39–63, 1956 (In Chinese).

Huang, M. H. and Huang, H. H.: The complexity of the 2018 Mw 6.4 Hualien earthquake in east Taiwan, Geophys. Res. Lett., 45, 13249–13257, https://doi.org/10.1029/2018GL080821, 2018.

Huang, M. W. and Wang, J. H.: Scaling of displacement spectra of near-fault seismograms of the 1999 Chi-Chi, Taiwan, earthquake, Geophys. Res. Lett., 29, 84-1–84-4, https://doi.org/10.1029/2001GL014021, 2002.

Huang, M. W. and Wang, J. H.: Scaled Energies of $M_L \geq 5.1$ Aftershocks of the 1999 Chi-Chi, Taiwan, Earthquake Measured from Local Seismograms, Terr. Atmos. Ocean. Sci., 20, 671-685, https://doi.org/10.3319/TAO.2008.10.13.01(T), 2009.

Huang, H. H. and Wang, Y.: Seismogenic structure beneath the northern Longitudinal Valley revealed by the 2018–2021 Hualien earthquake sequences and 3-D velocity model, Terr. Atmos. Ocean. Sci., 33, 17, https://doi.org/10.1007/s44195-022-00017-z, 2022.

Jia, Z., Jin, Z., Marchandon, M., Ulrich, T., Gabriel, A. A., Fan, W., Shearer, P., Zou, X., Rekoske, J., Bulut, F., Garagon, A., and Fialko, Y.: The complex dynamics of the 2023 Kahramanmaraş, Turkey, Mw 7.8-7.7 earthquake doublet, Science., 381, 985–990, https://doi.org/10.1126/science.adi0685, 2023.

Jian, P. R., Tseng, T. L., Liang, W. T., Huang, P. H.: A new automatic full-waveform regional moment tensor inversion algorithm and its applications in the Taiwan area, Bull. Seismol. Soc. Am., 108, 573-587, https://doi.org/10.1785/0120170231, 2018.

Jian, P. R. and Wang, Y.: Applying unsupervised machine-learning algorithms and MUSIC back-projection to characterize 2018–2022 Hualien earthquake sequence, Terr. Atmos. Ocean. Sci., 33, 28, https://doi.org/10.1007/s44195-022-00026-y, 2022.

King, G. C. P., Stein, R. S., and Lin, J.: Static stress changes and the triggering of earthquakes, Bull. Seismol. Soc. Am., 84, 935–953, https://doi.org/10.1785/BSSA0840030935, 1994.

Lee, S. J., Liu, T. Y., and Lin, T. C.: Slab tearing and break-off revealed by the 2024 M7.4 Taiwan earthquake, Geophys. Res. Lett., 52, e2025GL117826, https://doi.org/10.1029/2025GL117826, 2025.

Leonard, M.: Earthquake Fault Scaling: Self-Consistent Relating of Rupture Length, Width, Average Displacement, and Moment Release, Bull. Seismol. Soc. Am., 100, 1971–1988, https://doi.org/10.1785/0120090189, 2010.

Lin, Y. S., Chuang, R. Y., Yen, J. Y., Chen, Y. C., Kuo, Y. T., Wu, B. L., Huang, S.-Y., and Yang, C.-J.: Mapping surface breakages of the 2018 Hualien earthquake by using UAS photogrammetry, Terr. Atmos. Ocean. Sci., 30, 351-366, https://doi.org/10.3319/TAO.2018.12.09.02, 2019.

Lin, Y. Y., Kanamori, H., Zhan, Z., Ma, K. F., and Yeh, T. Y.: Modelling of pulse-like velocity ground motion during the 2018 Mw 6.3 Hualien earthquake, Taiwan, Geophys. J. Int., 348-365, https://doi.org/10.1093/gji/ggaa306, 2020.

Lin, C. W., Liu, Y. C., Chou, P. S., and Lin, Y. H.: Recent development of active fault investigations of Taiwan, Bull. Centr. Geol. Surv., 34, 1–40, 2021 (In Chinese).

Lin, Y. H. and Wu, Y. M.: Magnitude determination for earthquake early warning using P-alert low-cost sensors during 2024 Mw7.4 Hualien, Taiwan earthquake, Sci. Rep., 15, 12538, https://doi.org/10.1038/s41598-025-97748-z, 2025.

Pearson, K.: On lines and planes of closest fit to systems of points in space, Philos. Mag., 2, 559–572, https://doi.org/10.1080/14786440109462720, 1901.

Liu, C., Lay, T., Brodsky, E. E., Dascher-Cousineau, K., and Xiong, X.: Coseismic rupture process of the large 2019 Ridgecrest earthquakes from joint inversion of geodetic and seismological observations, Geophys. Res. Lett., 46, 11820–11829, https://doi.org/10.1029/2019GL084949, 2019.

Lo, Y. C., Yue, H., Sun, J., Zhao, L., and Li, M.: The 2018 Mw6.4 Hualien earthquake: dynamic slip partitioning reveals the spatial transition from mountain building to subduction, Earth Planet. Sci. Lett., 524, 115729, https://doi.org/10.1016/j.epsl.2019.115729, 2019.

Omori, F.: On the aftershocks of earthquake, J. Coll. Sci. Imp. Univ. Tokyo, *7*, 111–200, 1894.

Ouillon, G., Ducorbier, C., and Sornette, D.: Automatic reconstruction of fault networks from seismicity catalogs: Three-dimensional optimal anisotropic dynamic clustering, J. Geophys. Res., 113, B01306, https://doi.org/10.1029/2007JB005032, 2008.

Petersen, G. M., Büyükakpinar, P., Vera Sanhueza, F. O., Metz, M., Cesca, S., Akbayram, K., Saul, J., and Dahm, T.: The 2023 Southeast Türkiye Seismic Sequence: Rupture of a Complex Fault Network, Seism. Rec., 3, 134–143, https://doi.org/10.1785/0320230008, 2023.

Piegari, E., Camanni, G., Mercurio, M., and Marzocchi, W.:lluminating the hierarchical segmentation of faults through an Unsupervised Learning Approach applied to clouds of earthquake hypocenters, Earth Space Sci., 11, e2023EA003267, https://doi.org/10.1029/2023EA003267, 2024.

Piegari, E., Herrmann, M., and Marzocchi, W.: 3-D spatial cluster analysis of seismic sequences through density-based algorithms, Geophys. J. Int., 230, 2073–2088, https://doi.org/10.1093/gji/ggac160, 2022.

Quinn, D. P. and Ehlmann, B. L.: A PCA-based framework for determining remotely sensed geological surface orientations and their statistical quality, Earth Space Sci., 6, 1378-1408, https://doi.org/10.1029/2018EA000416, 2019.

Rau, R. J. and Wu, F. T.: Active tectonics of Taiwan orogeny from focal mechanisms of small-to-moderate-sized earthquakes, Terr. Atmos. Ocean. Sci., 9, 755–778, https://doi.org/10.3319/TAO.1998.9.4.755(TAICRUST), 1998.

Roden, R., Smith, T., and Sacrey, D.: Geologic pattern recognition from seismic attributes: Principal component analysis and self-organizing maps, Interpretation, 3, SAE59–SAE83, https://doi.org/10.1190/INT-2015-0037.1, 2015.

Rousseeuw, P. J.: Silhouettes: a graphical aid to the interpretation and validation of cluster analysis, J. Comput. Appl. Math., 20, 53–65, https://doi.org/10.1016/0377-0427(87)90125-7, 1987.

Savage, J. C.: Principal component analysis of geodetically measured deformation in Long Valley caldera, eastern California, 1983–1987, J. Geophys. Res., 93, 13297–13305, https://doi.org/10.1029/JB093iB11p13297, 1988.

Schubert, E., Sander, J., Ester, M., Kriegel, H. P., and Xu, X.: DBSCAN revisited, revisited: why and how you should (still) use DBSCAN, ACM Trans. Database Syst., 42, 19, 1–21, https://doi.org/10.1145/3068335, 2017.

Shyu, J. B. H., Sieh, K., Chen, Y. G., and Liu, C. S.: Neotectonic architecture of Taiwan and its implications for future large earthquakes, J. Geophys. Res., 110, B08402, https://doi.org/10.1029/2004JB003251, 2005.

Shyu, J. B. H., Chuang, Y. R., Chen, Y. L., Lee, Y. R., and Cheng, C. T.: A New On-Land Seismogenic Structure Source Database from the Taiwan Earthquake Model (TEM) Project for Seismic Hazard Analysis of Taiwan, Terr. Atmos. Ocean. Sci., 27, 311–323 https://doi.org/10.3319/TAO.2015.11.27.02(TEM), 2016.

Stein, R. S.: The role of stress transfer in earthquake occurrence, Nature, 402, 605–609, https://doi.org/10.1038/45144, 1999.

Stirling, M., Goded, T., Berryman, K., and Litchfield, N.: Selection of earthquake scaling relationships for seismic-hazard analysis, Bull. Seismol. Soc. Am., 103, 2993-3011, 2013.

Suppe, J.: Kinematics of arc-continent collision, flipping of subduction, and back-arc spreading near Taiwan, Geol. Soc. China. Mem., 6, 131–146, 1984.

Tang, C. H., Lin, Y. N., Tung, H., Wang, Y., Lee, S. J., Hsu, Y. J., Shyu, J. B. H., Kuo, Y. T., Chen, and H. Y.: Nearby fault interaction within the double-vergence suture in eastern Taiwan during the 2022 Chihshang earthquake sequence, Commun. Earth Environ., 4, 333, https://doi.org/10.1038/s43247-023-00994-0, 2023.

Toda, S., Stein, R. S., Richards-Dinger, K., and Bozkurt, S. B.: Forecasting the evolution of seismicity in southern California: Animations built on earthquake stress transfer, J. Geophys. Res., 110, B05S16, https://doi.org/10.1029/2004JB003415, 2005.

Tsai, Y. B.: Seismotectonics of Taiwan, Tectonophysics, 125, 17–37, https://doi.org/10.1016/0040-1951(86)90005-3, 1986.

Tung, H., Chen, H. Y., Hsu, Y. J., Hu, J. C., Chang, Y. H., and Kuo, Y. T.: Triggered slip on multifaults after the 2018 Mw 6.4 Hualien earthquake by continuous GPS and InSAR measurements, Terr. Atmos. Ocean. Sci, 30, 285–300, https://doi.org/ 10.3319/TAO.2019.04.03.01, 2019.

Wells, D. L. and Coppersmith, K. J.: New empirical relationships among magnitude, rupture length, rupture width, rupture area, and surface displacement, Bull. Seismol. Soc. Am., 84, 974–1002, https://doi.org/10.1785/BSSA0840040974, 1994.

Wen, S., Wen, Y. Y., Ching, K. E., Yeh, Y. L., and Lee, Y. H.: Tectonic implications on the 2018 Hualien Earthquake, Terr. Atmos. Ocean. Sci., 30, 389–398, https://doi.org/10.3319/TAO.2019.01.28.01, 2019.

Wu, Y. M., Chen, Y. G., Chang, C. H., Chung, L. H., Teng, T. L., Wu, F. T., and Wu, C. F.: Seismogenic structure in a tectonic suture zone: With new constraints from 2006 Mw6.1 Taitung earthquake, Geophys. Res. Lett., 33, L22305, https://doi.org/10.1029/2006GL027572, 2006.

Wu, Y. M., Shyu, J. B. H., Chang, C. H., Zhao, L., Nakamura, M., and Hsu, S. K.: Improved seismic tomography offshore northeastern Taiwan: Implications for subduction and collision processes between Taiwan and the southernmost Ryukyu, Geophys. J. Int., 178, 1042–1054, https://doi.org/10.1111/j.1365-246X.2009.04180.x, 2009.

Yen, J. Y., Lu, C. H., Dorsey, R. J., Kuo-Chen, H., Chang, C. P., Wang, C. C., Chuang, R. Y., Kuo, Y. T., Chiu, C. Y., Chang, Y. H., Bovenga, F., and Chang, W. Y.: Insights into seismogenic deformation during the 2018 Hualien, Taiwan, earthquake sequence from InSAR, GPS, and modeling, Seismol. Res. Lett., 90, 78–87, https://doi.org/10.1785/0220180228, 2019.

Yu, S. B., Chen, H. Y., and Kuo, L. C.: Velocity field of GPS stations in the Taiwan area, Tectonophysics, 274, 41–59, https://doi.org/10.1016/S0040-1951(96)00297-1, 1997.